# DIRECT NUMERICAL SIMULATION OF IMPULSIVELY STARTED, AND UNIFORMELY ACCELERATED, PLATES USING ADAPTIVE WAVELET AND FOURIER METHODS WITH PENALISATION

**Kai Schneider**[1,2,*], **Mickaël Paget-Goy**[1,3], **Giulio Pellegrino**[1],

**Alberto Verga**[4] **and Marie Farge**[5]

[1] Laboratoire de Modélisation et Simulation Numérique en Mécanique du CNRS
IMT - Technopôle de Château-Gombert
38 rue F. Joliot-Curie, 13541 Marseille Cedex 20, France

[2] Centre de Mathématiques et d'Informatique, Université de Provence
39 rue F. Joliot-Curie, 13543 Marseille Cedex 13, Marseille, France

[3] Ecole Supérieure de Mécanique de Marseille
IMT - Technopôle de Château-Gombert
13451 Marseille Cedex 20, France

[4] Institut de Recherche sur les Phénomènes Hors Equilibre
Technopôle de Château-Gombert
49 rue F. Joliot-Curie, 13384 Marseille Cedex 13, France

[5] Laboratoire de Météorologie Dynamique du CNRS, Ecole Normale Supérieure
24 rue Lhomond, 75231 Paris Cedex 05, France

## ABSTRACT

We present high resolution direct numerical simulation of 2D viscous incompressible flows past a flat plate. We study the shear layer instability of a flow past, either an impulsively started plate, or an uniformely accelerated plate, for Reynolds number $Re = 9500$. The numerical schemes are based on adaptive wavelet and Fourier pseudospectral methods with volume penalisation to take into account the plate with no–slip boundary conditions. The geometry of the plate is simply described by a mask function. We have chosen one tip of the plate to be rectangular while the other is a wedge with an angle of $30^o$ degrees or a circluar shape. On both tips we observe the formation of thin shear layers which are rolling up into spirals and form two primary vortices. The selfsimilar scaling of the spirals corresponds with theoretical predictions of Saffman for the inviscid case [12]. At later times these vortices are advected downstream and the free shear layers undergo a secondary instability. We show that their formation and subsequent dynamics is highly sensitive to the shape of the tips. The numerical results agree well with observations from laboratory experiments. Finally we also check the influence of a small riblet being added on the back of the plate on the flow evolution.

## INTRODUCTION

One of the main challenges in computational fluid dynamics (CFD) is the numerical simulation of turbulent flows in complex geometries. Grid generation and turbulence modeling near the wall play hereby a crucial point, especially for the prediction of lift and drag coefficients and for the control of the flow. A suitable approach for this task is the penalisation method which has been introduced by Arquis and Caltagirone [3]. Therewith walls or solid obstacles are modeled as a porous medium with porosity $\eta$ tending to zero. The Navier-Stokes equations are modified accordingly by adding a Darcy term. Fluid regions are considered as completely permeable, while regions where walls or obstacles are present as perfectly impermeable. The geometry of the flow can therefore simply be taken into account using a spatially varying permability coefficient, which enables an easy practical implementation of the method and allows furthermore obstacles and walls changing in time and even interacting with the fluid. A mathematical theory proving convergence of this physically based approach has been given by Angot, Bruneau and Fabrie [2]. The penalisation method has been applied in the context of low order methods (finite difference/volume schemes, e.g. [9, 2], with pseudospectral methods, e.g. [7], [8], [14] and recently also with adaptive wavelet methods [13], [6]. The latter scheme automatically adapts the spatial grid not only to the evolution of the flow, but also to the geometry of walls or bluff bodies [13].

In the present paper we apply the penalisation method using as numerical scheme, either a Fourier pseudo-spectral, or an adaptive wavelet method, to study the flow past a flat plate moving normal to the free stream. This flow configuration has been subject of many experimental, theoretical and numerical investigations [11, 12, 10]. Here we focus on the self-similar behaviour of the primary spiral vortex being formed at the sharp edges and we compare the numerical results with Saffman's theoretical predictions [12]. At later times, when the primary vortices are advected downstream, for sufficiently large Reynolds numbers, we observe the formation of secondary vortices along the primary vortex sheets. These results agree with observations in laboratory experiments [11] and with other numerical simulations using a vortex method [10]. The stability of vortex sheet roll–up

*kschneid@cmi.univ-mrs.fr

and its secondary instability has also been studied recently in [1].

The paper is organised as follows: first we present the penalisation method togehter with the numerical schemes to solve the penalised Navier-Stokes equations numerically. As application we present numerical simulations of 2D viscous incompressible flow around a flat plate, being either impulsively started normal to the free stream at $Re = 9500$, or uniformely accelerated. We also modify the plate's geometry by adding a small riblet to study its influence on the formation of the secondary vortices. Finally, we give some conclusions and perspectives for turbulence modeling.

## THE PENALISATION METHOD AND THE NUMERICAL DISCRETISATION

### Governing equations

The penalisation technique is based on the physical idea to model solid walls or obstacles as porous media whose porosity $\eta$ is tending to zero [3]. The geometry is described by a mask function $\chi(\vec{x})$ which is 1 inside the solid regions and 0 elsewhere. Note that the penalisation method can also take into account obstacles with time–varying shape by simply introducing a time–dependent mask function. The Navier-Stokes equations are modified by adding a supplementary term containing the mask function. For the 'penalised' velocity $\vec{u}_\eta$ we obtain

$$\partial_t \vec{u}_\eta + \vec{u}_\eta \cdot \nabla \vec{u}_\eta + \nabla p_\eta - \nu \nabla^2 \vec{u}_\eta + \frac{1}{\eta} \chi_{\Omega_s} (\vec{u}_\eta - \vec{u}_p(t)) = 0 \quad (1)$$

where $\vec{u}_\eta(\vec{x},t)$ is the velocity, $p_\eta(\vec{x},t)$ the pressure, $\vec{u}_p(t)$ the obstacle's velocity, and $\nu$ the kinematic viscosity. In the following the density $\rho$ is assumed to be 1. The mask function is given by

$$\chi_{\Omega_s}(\vec{x}) = \begin{cases} 1 & \text{for} \quad \vec{x} \in \bar{\Omega}_s, \\ 0 & \text{elsewhere} \end{cases} \quad (2)$$

where $\Omega_s$ denotes the solid obstacle. For $\eta \longrightarrow 0$ the flow evolution is governed by the Navier–Stokes equations in the fluid regions, and by Darcy's law, i.e. the velocity is proportional to the pressure gradient, in the solid regions where obstacles or walls are present. In [2] a mathematical proof has been given that the above equations converge towards the Navier–Stokes equations with no-slip boundary conditions, with order $\eta^{3/4}$ inside the obstacle and with order $\eta^{1/4}$ elsewhere, in the limit when $\eta$ tends to zero. In numerical simulations an improved convergence of order $\eta$ has been reported [2], [8].

The resulting forces $\vec{F}$ on the obstacle, i.e. drag and lift coefficients, can be computed by integrating the penalised velocity over the obstacle's volume [2]:

$$\vec{F} = \lim_{\eta \to 0} \int_{\Omega_s} \nabla p_\eta \, dx = - \lim_{\eta \to 0} \frac{1}{\eta} \int_{\Omega_s} \vec{u}_\eta \, dx \quad (3)$$

$$= \int_{\partial \Omega_s} \sigma(\vec{u}, p) \cdot \vec{n}_f \, d\gamma \quad (4)$$

where $\Omega_s$ is the obstacle's volume, $\partial\Omega_s$ its boundary, $\vec{n}$ its outer normal and $\sigma(\vec{u},p) = \frac{1}{2\nu}(\nabla\vec{u} + (\nabla\vec{u})^t) - pI$ the stress tensor. Hence the lift and drag forces on the obstacle, i.e. forces parallel and perpendicular to the free–stream velocity of the flow, are easy to compute as volume integrals instead of contour integrals.

For two–dimensional flows the vorticity–velocity formulation is prefered and therefore we take the curl of eq. (1), and we get

$$\partial_t \omega_\eta + (\vec{u}_\eta + \vec{U}_\infty) \cdot \nabla \omega_\eta - \nu \nabla^2 \omega_\eta + \nabla \times \left( \frac{1}{\eta} \chi_{\Omega_s} (\vec{u}_\eta) - \vec{u}_p(t) \right) = 0 \quad (5)$$

where $\omega = \nabla \times \vec{u}$ is the vorticity and $\vec{U}_\infty$ is the free–stream velocity, defined as $\lim_{|\vec{x}| \to \infty} \vec{u}(\vec{x}) = \vec{U}_\infty$.

### Numerical methods

For the numerical solution of the penalised equations we employ, either a classical Fourier pseudospectral method [4, 8, 14], or a wavelet scheme with adaptive grid refinement [6, 13].

#### Fourier pseudospectral method.

The Fourier pseudospectral discretizations are classical schemes in CFD, which are highly accurate for flows with periodic boundary conditions. For a more complete discussion we refer the reader to [4]. Equation (6) is transformed into Fourier space in order to compute the spatial derivatives and to evolve the vorticity field in time. Terms containing products, i.e. the convection and penalisation terms, are calculated by collocation in physical space. Hence the vorticity field and the other variables are represented as truncated Fourier series,

$$\omega(\vec{x},t) = \sum_{\vec{k} \in \mathbb{Z}^2} \widehat{\omega}(\vec{k},t) \, \exp(i\vec{k} \cdot \vec{x}) \quad (6)$$

where the Fourier transform of $\omega$ is defined as

$$\widehat{\omega}(\vec{k},t) = \frac{1}{4\pi^2} \int \omega(\vec{x},t) \, \exp(-i\vec{k} \cdot \vec{x}) \, d\vec{x} \quad (7)$$

with the wavevector $\vec{k} = (k_x, k_y)$. The Fourier discretization is uniform in space and is truncated at $k_x = -N_x/2$ and $k_x = N_x/2 + 1$, $k_y = -N_y/2$ and $k_y = N_y/2 + 1$, where $N_x$ and $N_y$ are the number of grid points in $x$ and $y$ direction, respectively. The gradient of $\omega$ is computed by multiplication of $\widehat{\omega}$ by $i\vec{k}$, the Laplacian by multiplication with $|\vec{k}|^2$. The velocity $\vec{u}$ induced by the vorticity $\omega$ is reconstructed in Fourier space using Biot-Savart's law,

$$\vec{u}(\vec{x},t) = \sum_{\vec{k} \in \mathbb{Z}^2, \vec{k} \neq 0} \frac{\vec{k}^\perp}{|\vec{k}|^2} \widehat{\omega}(\vec{k},t) \, \exp(i\vec{k} \cdot \vec{x}) \quad (8)$$

where $\vec{k}^\perp = (-k_y, k_x)$

The convection term $\vec{u} \cdot \nabla\omega$ and the penalisation term $\nabla \times (\frac{1}{\eta} \chi_{\Omega_s} (\vec{u} - \vec{u}_p(t))$ are evaluated by the pseudospectral technique using collocation in physical space. To avoid aliasing errors, i.e. the production of small scales due to the nonlinear terms which are not resolved on the grid, we de-aliase at each time step, by truncating the Fourier coefficients using the 2/3 rule,

$$\widehat{\omega}(\vec{k}) = \begin{cases} \widehat{\omega}(\vec{k}) & \text{for} \quad \left(\frac{3k_x}{2N_x}\right)^2 + \left(\frac{3k_y}{2N_y}\right)^2 < 1, \\ 0 & \text{for} \quad \left(\frac{3k_x}{2N_x}\right)^2 + \left(\frac{3k_y}{2N_y}\right)^2 \geq 1 \end{cases} \quad (9)$$

For the transformation between physical and Fourier space we use Temperton's Fast Fourier Transform with an order $\mathbf{N} \log_2 \mathbf{N}$, ($\mathbf{N} = N_x N_y$) complexity [4].

For the time discretization we use a semi-implicit scheme with adaptive time–stepping [14]. The linear diffusion term is discretized implicitly using exact time integration which is cheap for spectral methods, as the Laplace operator is diagonal in Fourier space, and hence no linear system has to be solved. This improves the stability limit of purely explicit schemes. The remaining terms are discretized explicitly using second order Adams–Bashforth extrapolation. This avoids the solution of nonlinear equations, however it implies a CFL condition on the maximum size of the time step.

The step size control of the time step is based on the CFL stability limit of the explicit discretization of the nonlinear term. Therefore in each time step $t_n$, pointwise the maximal rms velocity is computed,

$$u_{max} = max_{\vec{x}} \quad \sqrt{(u(\vec{x}))^2 + (v(\vec{x}))^2} \tag{10}$$

and the new time step is given by

$$\Delta t_{n+1} = C\Delta x / u_{max}$$

with the minimal spatial grid size $\Delta x = \min\left(\frac{L_x}{N_x}, \frac{L_y}{N_y}\right)$, where $L_x, L_y$ denote the length of the domain in $x$ and $y$ direction, respectively, and $C < 1$ the CFL constant.

**Adaptive wavelet method.**

As adaptive schemes dynamically adapt the spatial grid in time, we first discretize the equations (6) in time using semi-implicit finite differences, i.e. Euler–backwards (EB2) for the viscous term and Adams–Bashforth (AB2) extrapolation for the nonlinear term, which are both of second order.

The resulting elliptic problem to be solved in each time step is:

$$(\gamma I - \nu\nabla^2)\omega^{n+1} = \frac{4}{3}\gamma\omega^n - \frac{1}{3}\gamma\omega^{n-1} - \nabla\cdot(\omega^\star\,\vec{u}^\star) \quad (11)$$
$$-\nabla\times(\frac{1}{\eta}\,\chi\,(\vec{u}^\star - \vec{u}_p))$$

where

$$\omega^\star = 2\,\omega^n - \omega^{n-1} \qquad \vec{u}^\star = 2\,\vec{u}^n - \vec{u}^{n-1} \tag{12}$$

and with time step $\Delta t$, $\gamma = 3/(2\Delta t)$ and $I$ representing the identity.

For the space discretization we use a Petrov–Galerkin scheme. Therefore the vorticity is developed into a set of trial functions and the minimization of the weighted residual of (11) requires that the projection onto a space of test functions vanishes. As space of trial functions we employ a two-dimensional multiresolution analysis (MRA) and develop $\omega^n$ at time step $n$ into an orthonormal wavelet series

$$\omega^n(x,y) \;=\; \sum_\lambda \langle\omega^n\,,\,\psi_\lambda\rangle\;\psi_\lambda(x,y) \tag{13}$$

with the multiindex $\lambda = (j, i_x, i_y, \mu)$, where $j = 0, J_{max} - 1$ denotes the scale $2^{-j+1}$, $(i_x, i_y) = 0, ..., 2^j - 1$ the position and $\mu = 1, 2, 3$ the three different directions of the wavelets. The test functions $\theta_\lambda$ are defined as solutions of the linear part of eq. (11)

$$(\gamma I - \nu\nabla^2)\theta_\lambda \;=\; \psi_\lambda \tag{14}$$

and can be computed in a preprocessing step.

This avoids assembling the stiffness matrix and solving a linear equation at each time step. The functions $\theta$, called vaguelettes, are explicitely calculated in Fourier space and have similar localization properties as wavelets [6]. The solution of (11) therewith reduces to a change of basis:

$$\begin{aligned}\tilde{\omega}_\lambda &= \langle\omega^{n+1}\,,\,\psi_\lambda\rangle \\ &= \langle(\frac{4}{3}\gamma\omega^n - \frac{1}{3}\gamma\omega^{n-1} - \nabla\cdot(\omega^\star(\vec{u}^\star)) \\ &- \nabla\times(\frac{1}{\eta}\chi(\vec{u}^\star - \vec{u}_p))), \theta_\lambda\rangle \quad .\end{aligned} \tag{15}$$

Nonlinear wavelet thresholding is applied in each time step to obtain an adaptive discretization by retaining only those wavelet coefficients $\tilde{\omega}_\lambda$ with absolute value above a given threshold $\epsilon = \epsilon_0\sqrt{Z}$, where $\epsilon_0$ is a constant and $Z = \frac{1}{2}\int|\omega(\vec{x})|^2 d\vec{x}$ is the enstrophy. For the next time step the index coefficient set (which addresses each coefficient in wavelet space) is determined by adding neighbours to the retained wavelet coefficients. Consequently, only those coefficients $\tilde{\omega}$ in (15) belonging to this extrapolated index set are computed using the adaptive vaguelette decomposition [6]. The nonlinear term $-\nabla\cdot(\omega^\star(\vec{u}^\star)) - \nabla\times(\frac{1}{\eta}\,\chi\,(\vec{u}^\star - \vec{u}_p))$ is evaluated by partial collocation on a locally refined grid [13]. The vorticity $\omega^\star$ is reconstructed in physical space on an adaptive grid from its wavelet coefficients $\tilde{\omega}^\star$ using the adaptive wavelet reconstruction algorithm [6]. From the adaptive vaguelette decomposition with $\theta = (\nabla^2)^{-1}\,\psi$, we solve $\nabla^2\Psi^\star = \omega^\star$ to get the stream function $\tilde{\Psi}^\star$ and reconstruct $\Psi^\star$ on a locally refined grid. By means of centered finite differences of 4th order we compute $\nabla\omega^\star$, $\vec{u}^\star = (-\partial_y\Psi^\star, \partial_x\Psi^\star)$ and $\nabla\times(\frac{1}{\eta}\,\chi\,(\vec{u}^\star - \vec{u}_p))$ on the adaptive grid. Subsequently, the nonlinear term is summed up pointwise and finally (15) is solved using the adaptive vaguelette decomposition.

## NUMERICAL RESULTS

**Flow configuration**

We study the early evolution of incompressible viscous flows past a flat plate. The plate is deplaced in its normal direction (Fig. 1), with a motion being, either impulsively started, or uniformely accelerated. We have chosen one tip of the plate to be rectangular while the other is a wedge with an angle of $30^o$ degree (cf. Fig. 1). The two-dimensional approximation, we use here, remains valid, since we focus on the instationary flow behaviour at early times. At $t = 0$

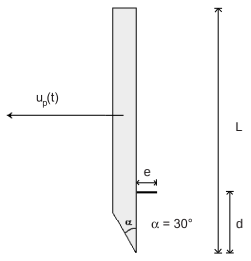


Figure 1: Geometry of the flat plate and direction of its motion.

the plate is either impulsively started

$$\vec{u}_p(t) \;=\; \begin{cases} u_0 & t \geq 0, \\ 0 & t > 0 \end{cases} \tag{16}$$

with velocity $u_0 = 1$, or uniformely accelerated with velocity

$$\vec{u}_p(t) = \begin{cases} at & t \geq 0, \\ 0 & t > 0 \end{cases} \quad (17)$$

with the acceleration $a = 1$. Based on the length of the plate $L$ we define a Reynolds number $Re = \frac{u_p L}{\nu}$ which evolves in the uniformely accelerated case with time.

**Spiral formation at early times**

The flow past a flat plate has been studied theoretically using potential flows in the complex plane [12]. A Kutta condition is imposed at the tip of the plate by adding a spiral vortex to the potential flow (see Fig. 2). In [12] a self-similar scaling of the spiral is predicted, which depends on the angle of the wedge $\alpha$ and the acceleration law of the plate. The numerical simulations are performed with resolution $N_x = N_y = 2048$. In Fig. 3 we show the vorticity field at $t = 1.4$ for the impulsively started plate at $Re = 9500$. The flow is characterized by the roll-up of the two free shear layers produced at the tips into two counter-rotating primary vortices behind the plate. The resulting large scale recirculation zones create two boundary layers on the back of the plate, separated by a stagnation point located in the middle. These boundary layers produce vorticity, of opposite sign to the primary vortices, and form a corner vortex at each tip of the plate. Fig. 3 also exhibits secondary vortices resulting from an instability of the two shear layers. We observe that the shape of the tips (square shape on the top, and sharp edge on the bottom) strongly influences this secondary instability, since the spatial distribution of secondary vortices differs significantly. For the sharp edge (bottom) the distance between two subsequent vortices is continuously increasing, from the edge to the center of the primary vortex, where they disappear under the straining of the latter. In contrast, we observe for the square edge (top) an irregular distribution of the secondary vortices, whose strength remains sufficient to resist the straining of the primary vortex and hence they penetrate towards its center.

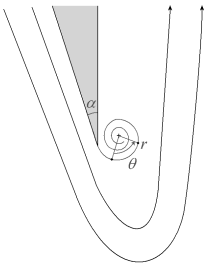


Figure 2: Sketch of the flow configuration.

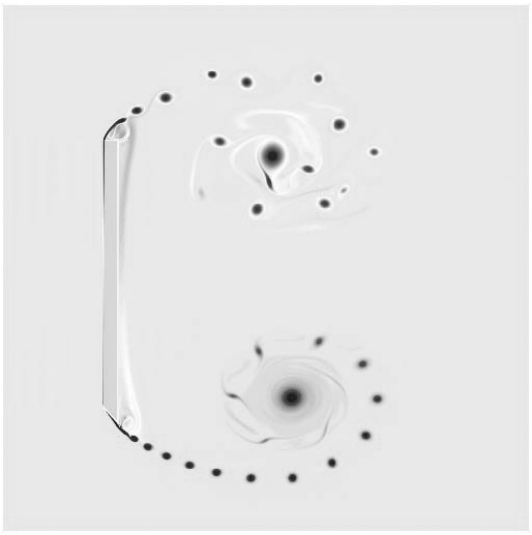

Figure 3: Vorticity field at $t = 1.4$ for the impulsively started plate at $Re = 9500$.

In the following we study the formation and roll-up of the shear layer and focus on the lower half of the plate with a wedge of $\alpha = 30^o$. In Fig. 6 we show the time evolution of vorticity.

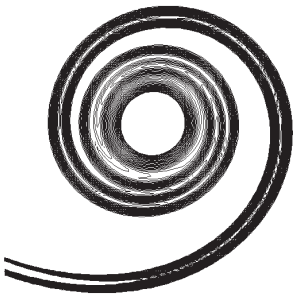

Figure 4: Zoom of the primary vortex spiral at $t = 0.4$ for an impulsively started plate at $Re = 9500$. Isolines of vorticity (-100,-10 by step of 2).

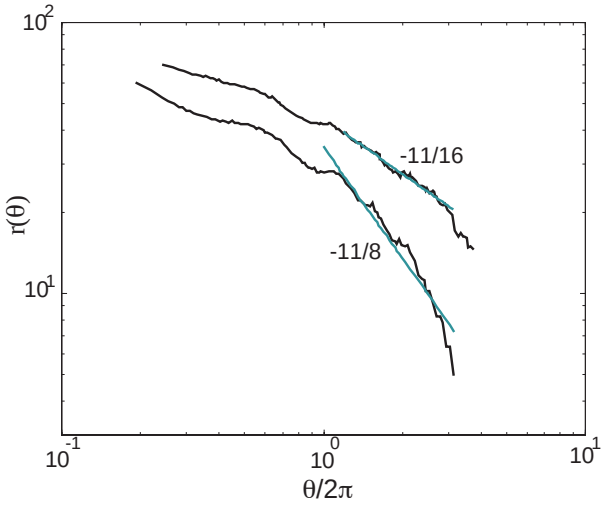


Figure 5: Scaling of the spiral's radius versus the angle $\theta$ for both the impulsively started (curve with slope $-11/16$) and for uniformely accelerated case (curve with slope$-11/8$ ).

At early times we observe the formation of a thin vortex sheet which is rolling up into a spiral and forms a primary vortex (Fig. 6, top). Fig. 4 shows a zoom of the spiral (case $\alpha = 30^o$) at early time ($t = 0.4$), i.e. we plot isolines of the vorticity field to study the scaling of the spiral vortex. In Fig. 5 we plot the scaling of the spiral's radius for both, the impulsively started and the uniformely accelerated case. For both we observe a self-similar behaviour with a scaling

of $r(\theta) \propto \theta^{-11/8}$ for the former, and of $r(\theta) \propto \theta^{-11/16}$ for the latter. The results agree well with Saffman's predictionfor the inviscid case, i.e. for infinite Reynolds numbers, [12] concerning the roll up of vortex sheets for an accelerated flow past a wedge with the same angle. Note that the impulsively started flow corresponds to the limit case of an infinite acceleration which is also well predicted.

**Formation of secondary vortices at later times**

The primary vortices being formed on the upper and lower tip are advected downstream. For sufficiently large Reynolds numbers ($Re > 5000$) we observe that the shear layers undergo a secondary instability at later times. This instability leads to the formation of secondary vortices along the primary vortex sheets (Fig. 6 and 3) as observed in both laboratory and numerical experiments, at similar Reynolds numbers [10, 15]. We also observe that the formation of the


Figure 6: Flow past an impulsively started plate with a sharp wedge of angle $\alpha = 30^o$ at $Re = 9500$. Vorticity fields at $t = 0.39, 0.75, 1.11$ and $1.47$.

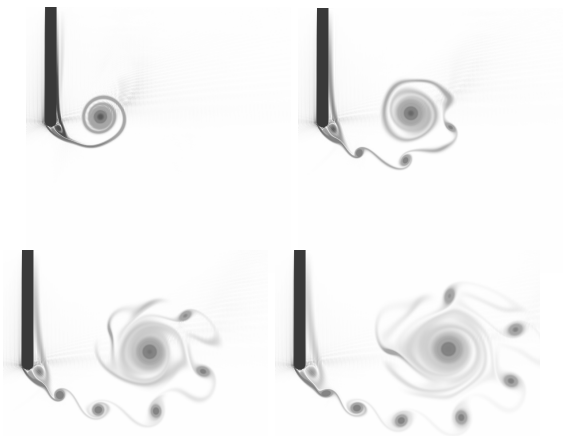

Figure 7: Flow past an impulsively started plate with a round wedge at $Re = 9500$. Vorticity at $t = 0.39, 0.75, 1.11$ and $1.47$.

secondary vortices and their dynamics are highly sensitive to the shape of the tips. Therefore we consider two different wedges, a sharp one with angle $\alpha = 30^o$ and a smooth one with a circular shape. We compare the corresponding flow evolution and we find that the formation of the secondary instability is delayed in the case of the sharp edge, i.e. at t = 0.75 no secondary vortices are observed (Fig. 6, top, right), while they are already well formed in the case of the round wedge (Fig. 7, top, right). For a square shaped edge (not shown here) we have observed that the secondary instability occurs even slightly earlier than for the round edge. This suggests that the position of the separation point seems to control the onset of the instability. This point is displaced depending on the shape of the wedge: from the left for the square, towards the middle for the round, to the right for the sharp edge. Correspondingly the position of the counter-rotating corner vortex is displaced likewise, from the left to the right. In [15] it has been suggested that this corner vortex triggers the secondary instability, which is consistent with our observations above. They also conjectured that the periodicity of the secondary vortex formation corresponds to the rotation frequency of the corner vortex.

In order to control the intensity of the corner vortex, and therefore its rotation frequency, we added a riblet on the back of the plate. As the riblet is in the recirculation zone behind the plate (cf. Fig. 1), it produces vorticity of the same sign as the corner vortex. We thus control its intensity, by varying the position $d$ and the size $e$ of the riblet, and performed several numerical experiments to check the riblet's influence on the secondary instability. In Fig. 8 we show the vorticity field at $t = 2.01$ without riblet (top, left) and for three different riblet positions. We observe that the dynamics of the secondary vortices is modified by the riblet. For increasing ratio $d/L$, we find that:

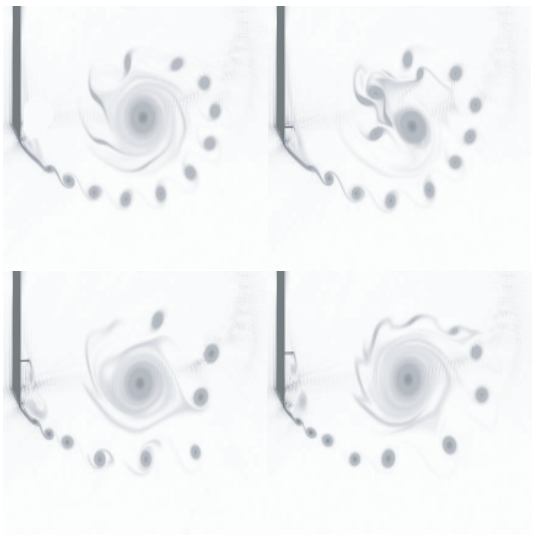

Figure 8: Flow past an impulsively started plate with a sharp wedge, angle $\alpha = 30^o$ at $Re = 9500$. Vorticity fields at $t = 2.01$ for a plate without riblet (top, left), and for plates with riblets at different positions.

- the formation of the first secondary vortex is getting closer to the tip of the plate,
- the distance between two secondary vortices becomes irregular,
- therefore vortex pairings occur.

We have also studied the influence of the Reynolds number in the range between $Re = 1000$ to $Re = 20000$ and for different position, size and thickness of the riblet. This will be discussed in a forthcoming paper.

## CONCLUSION AND PERSPECTIVES

We presented numerical simulation of 2D incompressible viscous flows past a flat plate at $Re = 9500$. A volume penalisation approach is used to take into account the geometry of the plate with no-slip boundary conditions. We used two different numerical schemes, either a Fourier pseudospectral method, or an adaptive wavelet method, both at high resolution ($\mathbf{N} = 2048^2$). Therewith we have studied numerically the free shear layer instability of a flow past a flat plate for different shapes of the tips. We found that the roll-up of the shear layer into a spiral, which forms the starting vortex, exhibits the scaling laws predicted by Saffman [12] for both cases studied here, the impulsively started and the uniformely accelerated plate. At later times we observed that the shear layer becomes unstable and produces secondary vortices as observed in both, laboratory and numerical, experiments. We also showed that the formation of the secondary vortices depends on the shape of the tips of the plate, and is enhanced by adding a riblet on its back. By varying the position and the size of the riblet we showed that the dynamics of the secondary vortices can be modified. The next step will be to develop systematic control strategies of the wake to enhance, but also to inhibit, their formation. In future work, we will also apply the CVS approach to compute 2D and 3D bluff body flows at higher Reynolds numbers [5].

**Acknowledgements:** We thank Thomas Leweke for fruitful discussions.

*

References

[1] M. Abid and A. Verga. Stability of a vortex sheet roll–up. *Phys. Fluids.*, 2003, in press.

[2] P. Angot, C.-H. Bruneau and P. Fabrie. A penalisation method to take into account obstacles in viscous flows. *Num. Math.*,**81**, 497–520, 1999.

[3] E. Arquis and J.P. Caltagirone. Sur les conditions hydrodynamiques au voisinage d'une interface milieu fluide – milieux poreux: application à la convection naturelle. *C. R. Acad. Sci. Paris II*, **299**, 1–4, 1984.

[4] C. Canuto, M.Y. Hussaini, A. Quaternioni and T. A. Zang. *Spectral Methods in Fluid Dynamics*, Springer-Verlag, Berlin Heidelberg, 1988.

[5] M. Farge and K. Schneider. Coherent Vortex Simulation (CVS), a semi–deterministic turbulence model using wavelets. *Flow, Turbulence and Combustion*, **66**(4), 393–426, 2001.

[6] J. Fröhlich and K. Schneider. An adaptive wavelet–vaguelette algorithm for the solution of PDEs. *J. Comput. Phys.*, **130**, 174–190, 1997.

[7] M. Forestier, R. Pasquetti and R. Peyret. Calculations of 3D wakes in stratified fluids. *ECCOMAS*, 2000.

[8] N. Kevlahan and J.-M. Ghidaglia. Computation of turbulent flow past an array of cylinders using a spectral method with Brinkman penalization. *Eur. J. Mech./B*, **20**, 333–350, 2001.

[9] K. Khadra, S. Parneix, P. Angot and J.-P. Caltagirone. Fictious domain approach for numerical modelling of Navier–Stokes equations. *Int. J. Num. Meth. Fluids*, **34**, 651–684, 2000.

[10] P. Koumoutsakos and D. Shiels. Simulations of the viscous flow normal to an impulsively started and uniformely accelerated flat plate. *J. Fluid. Mech.*, **328**, 177–227, 1996.

[11] D. Pierce. Photographic evidence of the formation and growth of vorticity behind plates accelerated from rest in still air. *J. Fluid. Mech.*, **11**, 460–464, 1961.

[12] P.G. Saffman. Vortex Dynamics. *Cambridge University Press*, 1993.

[13] K. Schneider and M. Farge. Adaptive wavelet simulation of a flow around an impulsively started cylinder using penalisation. *Appl. Comput. Harm. Anal.*, **12**, 374–380, 2002.

[14] K. Schneider. Direct numerical simulation of the transient flow behaviour in chemical reactors using a penalisation method. *Comput. Fluids*, submitted.

[15] Z.J. Wang, J.G. Liu and S. Childress. Concection between corner vortices and shear layer instability in flow past an ellipse. *Phys. Fluids*, **11**(9), 2446–2448, 1999.